Reaction Chemistry & Engineering

On the Redox Mechanism of Methanol Carbonylation on the Dispersed ReO_x/SiO_2 Catalyst

Journal:	*Reaction Chemistry & Engineering*
Manuscript ID	RE-ART-10-2024-000496.R1
Article Type:	Paper
Date Submitted by the Author:	16-Dec-2024
Complete List of Authors:	Tran, Neil; University of Illinois Urbana-Champaign, Chemical and Biomolecular Engineering Mironenko, Alexander; University of Illinois Urbana-Champaign, Chemical and Biomolecular Engineering

On the Redox Mechanism of Methanol Carbonylation on the Dispersed ReO_x/SiO_2 Catalyst

Neil D. Tran and Alexander V. Mironenko*
Department of Chemical and Biomolecular Engineering, University of Illinois Urbana-Champaign, Urbana, Illinois 61801, United States
*Email: alexmir@illinois.edu

Abstract:
Acetic acid is industrially produced by methanol carbonylation using Ir- or Rh-based homogeneous catalysts and a corrosive HI promoter. Recently, a heterogeneous catalyst with atomically dispersed ReO_4 sites on an inert mesoporous SBA-15 support demonstrated high acetic acid yields and stability without the need for a promoter (Qi et al. *J. Am. Chem. Soc.* 2020, 142, 14178). In this study, we investigate the reaction mechanisms of methanol carbonylation on monopodal -$ORe(=O)_3$ sites using density functional theory calculations, natural bond orbital analysis, and the energetic span model. We find that the reduction of dispersed Re(VII) oxide by CO through an indirect mechanism is essential for catalyst activation. The C–C coupling of methyl and carbonyl ligands is favorable in both Re(V) and Re(III) complexes, with Re(III) being superior due to transition state stabilization by a metal-localized lone electron pair. The preceding C–O bond activation is favorable only on Re(V) and leads to a thermodynamic sink, posing challenges in interpreting the high carbonylation activity in terms of monopodal ReO_x site catalysis. We hypothesize that multi-nuclear sites or more exotic ligand environments drive the cooperative reaction mechanism of selective carbonylation.

Keywords: methanol carbonylation, acetic acid, rhenium oxide, heterogeneous catalysts, redox mechanism

1. Introduction

Acetic acid (AA) is one of the ten most produced commodity chemicals, with annual production reaching 18.71 million tons in 2024.[1] It is a key intermediate in the production of polyvinyl acetate-based adhesives, alkyl acetates, acetic anhydride, and serves as a solvent in the synthesis of terephthalic acid.[2] More than 85% of AA available on the world's market is produced by means of methanol (MeOH) carbonylation using homogeneous catalysts.[2] The current Ir-based Cativa process,[3-6] which is economically superior to earlier Rh-based Monsanto[7-12] and Co-based BASF[13] technologies, requires energy-intensive separation of expensive homogeneous complexes $[IrI_2(CO)_2]^-$ and $[RuI_2(CO)_3]$. Additionally, it employs an iodide promoter to convert a strong CH_3-OH bond into a weaker, easy-to-activate CH_3-I bond, at the cost of generating corrosive hydriodic acid that imposes stringent corrosion resistance requirements on materials for reactor walls. Consequently, there has been interest in reducing separation costs by immobilizing the catalyst on a heterogeneous support and exploring new catalytic systems that would minimize or eliminate the use of the corrosive promoter. Past, present, and emerging MeOH carbonylation technologies have been recently reviewed.[2, 14]

Grafting ultradisperse ligated metal centers ML_n (where M is Rh, Ir, Au,[15, 16] or Pt[17]) onto surfaces (denoted by A) enables tuning of both catalyst stability and activity through variations of the strength of the $L_{n-m}M - X_m/A$ chemical bonds and by introducing new functionalities in X. Here, X is either a surface-bound species or an exposed structural motif of A. This strategy not only facilitates catalyst separation but often results in catalytic activity of grafted sites that is claimed to exceed that of homogeneous

counterparts.[18, 19] The explored design space of X/A for supporting the Rh or Ir sites includes activated carbon (AC) with and without N,S-codoping,[19-22] La-promoted[23-25] and La/SO_4^{2-}-promoted[26] AC, AC impregnated with $RhCl_3$ and an iodine compound,[27] polymers,[18, 28-32] C_3N_4,[33, 34] zeolites,[35] and heteropolyacids.[36-38] Despite the promising performance, the effect of the $M-X_m/A$ bond on the M electronic structure is typically too weak to enable the direct cleavage of the CH_3-OH bond without the need for the iodide promoter, or to substitute expensive Rh and Ir with lower-cost alternatives. Using base metals[39-41] or mimicking the promoter effect by ZrO_2 with tuned acidity[42] or a W-based heteropolyacid[43, 44] results in only modest AA or methyl acetate (MA) selectivities. An exception is $NiCl_2/CuCl_2$/C modified with CeO_2, which demonstrates 87% selectivity to MA.[45]

A widely explored iodide-free, noble-metal-free carbonylation process utilizes Brønsted acidic sites located inside the 8-member-ring (8-MR) pockets of specific zeolites, such as mordenite,[46-51] T zeolite,[52] and EU-12,[53] using MeOH, methyl chloride, or dimethyl ether (DME) as a reactant. For MeOH and DME, the reaction starts with the C-O bond cleavage, enabled by the protonation of an OH (or OCH_3) group, forming a good leaving group (H_2O or CH_3OH) and a surface-bound CH_3^+. The latter undergoes a nucleophilic attack by CO along the preferential direction inside the 8-MR channel[54] through the Koch-type reaction, forming an acylium ion that gets hydrolyzed to AA. Activation of CO by Cu^+ sites increases the reaction rate and steers the chemistry toward MA formation.[55-58] Due to the high, non-self-limiting carbocation reactivity, it is essential to passivate Brønsted acidic sites in larger 12-MR pores by bulky bases (such as pyridine) in order to limit the growth of coke-generating species.[46] Challenges associated with low yields, transport limitations in narrow pores, high CO:MeOH ratios, and catalyst stability must be addressed prior to commercial use of this technology.

Metal oxides have recently gained increasing attention as a class of heterogeneous catalysts for halide-free methanol carbonylation. The described catalytic systems include Ni-doped MoO_x,[59] Cu^+/TiO_2-SiO_2,[60] Cu^+/Sn-β,[61] and ultradispersed ReO_x on an SBA-15 amorphous silica support.[62] In analogy with oxide-catalyzed redox processes, the CH_3-OH bond activation on such catalysts may proceed through the reverse Mars-van Krevelen mechanism on partially reduced surfaces,[63-66] which may not require the use of a promoter due to high oxophilicity of vacancy sites on less reducible oxides with strong M-O bonds.[67] The vacancy- or reduced-state-mediated mechanism is potentially consistent with the methanol carbonylation activity of the traditional CoMoS hydrodesulfurization catalyst[68] and the hydrodeoxygenation activity of ReO_x.[69]

Among the reported metal oxide systems, the ReO_x/SiO_2 catalyst, described by Qi, Christopher, and coworkers,[62] is particularly promising. Combining single site grafting with metal oxide chemistry, it can achieve over 93% selectivity toward AA and 60% conversion of MeOH during a 60-hour reaction period. Catalyst activity further increases upon the addition of ~0.2 wt% of dispersed Rh, becoming comparable to the homogeneous processes.[62] Despite the impressive performance of this catalyst, it remains challenging to identify the structure of the catalytic site associated with the reported activity using experimental techniques.[70] Also, elementary reaction steps remain largely unknown. Open structural and mechanistic questions can be addressed with first-principles computational methods, which can help unravel the atomistic picture of this catalyst, elucidate each elementary step of the catalytic cycle, thereby enabling catalyst tuning and guiding the controlled synthesis of the catalyst.

In this work, we conduct a comprehensive quantum-mechanical investigation of methanol carbonylation to acetic acid on the silica-supported single-site $OReO_3/SiO_2$ catalyst. Using density functional theory (DFT) calculations, natural bond orbital (NBO) analysis, and the energetic span model,

we examine the reactivity of surface species in various coordination environments. First, we rule out previously reported reaction mechanisms and establish that the -$OReO_3$ catalytic site requires activation through reduction. Next, we investigate reactivity trends as a function of ligand environments in three hypothesized elementary steps that parallel those in Monsanto and Cativa processes: C-O bond scission, C-C coupling, and C-O bond formation. We find that the essential C-C coupling step is kinetically favorable in both Re(V) and Re(III) complexes, with Re(III) being preferred due to transition state (TS) stabilization by a metal-localized lone electron pair. The subsequent C-O coupling of -$COCH_3$ with -OH is more kinetically facile than with =O to form acetate. The C-O scission step preceding the C-C bond formation is favored on Re(V) but leads to an inactive Re(VII) complex. The C-O bond activation on Re(III), although compatible with the subsequent Re(V)-catalyzed C-C bond formation, exhibits too high a barrier due to an electron-withdrawing CO ligand. Thus, we find that the C-O scission and C-C formation steps require disparate oxidation states and ligand environments that are difficult to reconcile, revealing challenges in interpreting high methanol carbonylation activity on ReO_x/SiO_2 in terms of monopodal catalytic sites. Our results highlight the need to consider multinuclear sites or more exotic ligand configurations to explain the efficient carbonylation catalysis on ReO_x/SiO_2.

2. Computational methods

a. Catalytic site model

To develop a model for the catalytic site bound to the amorphous SBA-15 support, we started with a ~10,000-atom slab model of hydrated vitreous silica generated with molecular dynamics by Garofalini,[71] which accurately reproduces the experimental structure factor from neutron diffraction,[72] the average experimental Si-O distance, and average O-Si-O and Si-O-Si angles.[73-76] Its surface silanol group density (6.4 OH/nm^2) is close to the range observed in hydroxylated SiO_2 surfaces (4.2-5.7 OH/nm^2)[73, 77, 78] and is slightly greater than the value in SBA-15 (3.7 OH/nm^2 [79]).

In this study, we considered a monopodal (i.e., associated with a single siloxo group[80]) surface-bound trioxo Re(VII) species, denoted as $OReO_3$. Certain metals tend to favor a bipodal configuration[81] associated with hydrogen-bonded silanol pairs on amorphous silica,[82] which undergo condensation with hydroxyls of a metal precursor ($-MOH + -SiOH \rightarrow M-O-Si + H_2O$). This possibility, however, is likely ruled out for $OReO_3/SiO_2$ by processes and interactions that occur during catalyst synthesis. In an aqueous mixture of a precursor solution and an SBA-15 suspension,[62] the perrhenic acid (Re precursor) [$O_3Re{-}O{-}ReO_3(H_2O)_2$] exists as an anionic species non-covalently bound to the SiO_2 surface[83] and thus does not undergo condensation with the silanol pairs. Our DFT calculations also indicate the condensation of MOH and SiOH to be endergonic by 0.06 eV and thus unfavorable in water excess (Figure S1). During subsequent temperature pretreatment, dry perrhenic acid starts to decompose to Re_2O_7 and H_2O and lose its hydroxyls already at 100°C, when the equilibrium water vapor pressure reaches 0.02 atm, further raising to 0.5 atm at

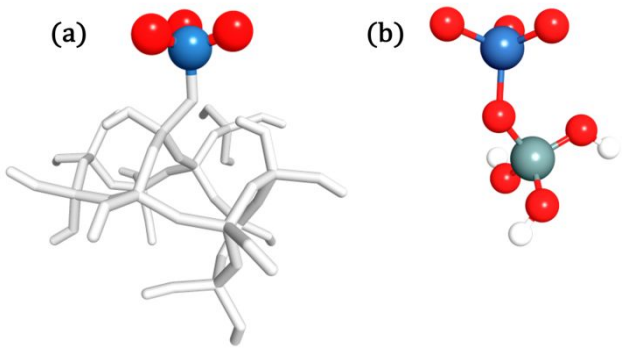

Figure 1. A single-site ReO_4 attached to an amorphous silica support: (a) a large cluster model; (b) a small cluster model with the -$OSi(OH)_3$ group representing the support. Blue is rhenium, red is oxygen, green is silicon, white is hydrogen. The white backbone represents the amorphous silica structure.

200°C.[84] Similarly, at 300°C, ~30% of surface silanol groups are converted to Si-O-Si siloxane bridges, with the fraction of converted groups increasing to ~60% at 500°C,[85] mainly due to the loss of silanol pairs.[82] The newly formed Re-O-Re units and Si-O-Si siloxanes mutually react at 350°C, yielding monopodal trioxo rhenium species -Si-O-ReO_3, as was established by Scott and Basset.[86] Dehydration of hydroxyls and formation of Si-O-Re motifs are thus substantial during catalyst calcination at 450°C,[62] making the formation of bipodal rhenium unlikely and favoring monopodal sites. The existence of SiO_2-supported monopodal $-OReO_3$ was confirmed using in situ IR, UV-vis, and in situ Raman spectroscopy with $^{18}O/^{16}O$ isotopic exchange by Lee and Wachs.[87, 88] The monopodal computational model is also consistent with *in situ* Re L3-edge XANES and EXAFS spectra[89] (Table S1).

In this work, a computationally tractable model of a SiO_2-anchored trioxorhenium was developed by replacing a randomly chosen surface silanol group on a vitreous silica slab with a $-O-ReO_3$ motif, followed by carving a ~70 atom cluster (Figure 1a) at the converged radius, as described in Section S1. Dangling bonds on oxygen atoms were terminated with hydrogen 0.97 Å away in the direction of the cleaved bond. Dangling bonds on silicon atoms were avoided by recovering neighboring O atoms and capping them with H. Among several surface silanols, only one was considered for Re binding, as the properties of monopodal species are largely independent of the silanol group position and its environment.[81] To further reduce the computational cost, a simplified $(OH)_3Si$-O-ReO_3 cluster with fixed H atoms was constructed (Figure 1b). By comparing geometric and CO chemisorption properties of both cluster models (Tables S1 and S2), we conclude that the simplified cluster provides a chemically and structurally accurate representation of the larger ~70 atom cluster at much lower computational cost. To validate the simplified model further, -O-ReO_3 was grafted onto three randomly selected silanol groups, with the support truncated at the third-nearest neighbor oxygen atom. The geometric properties were consistent across all structures, and the activation barriers for the model reaction (C–C coupling of $Re(=O)(CH_3)(CO)(OH)$, see Section 3b) showed good agreement among the different models (Table S3). Thus, the $(OH)_3Si$-O-ReO_3 model is used for the majority of calculations in this work.

b. DFT calculations

Calculations of geometries, energies, and vibrational frequencies of reaction intermediates and transition states (TS) were carried out using Kohn-Sham density functional theory (DFT) as implemented in ORCA 5.0.4.[90] We used the large basis set ma-def2-TZVP[91] and the ωB97X-D[92] hybrid functional that incorporates the D3 dispersion correction[93] with Becke-Johnson damping.[94, 95] The RIJCOSX – including RI-J approximation for Coulomb integrals[96-98] and the chain-of-spheres COSX numerical integration for HF exchange[99] – and AutoAux options were enabled to speed up calculations. In the initial optimization of the catalyst cluster, O atoms of terminal hydroxyls were fixed. In calculations for elementary reaction steps, the cluster was fixed except three nearest neighbors of the O atom underneath ReO_3. Reaction intermediates and the ReO_x species were fully relaxed. Both singlet and triplet states for each elementary step were considered. The lowest-energy spin state for reactants, TS, and products were chosen with the assumption of spin-crossing being fast and not rate-limiting.

In a typical TS calculation, we first generated a minimum energy pathway using the climbing-image nudged elastic band (CI-NEB) method[100, 101] to obtain an initial guess for the saddle point. Subsequently, the eigenvector-following algorithm ("OptTS")[102] was employed to converge on the true TS. The TS structure was validated by the presence of a single imaginary frequency corresponding to the reaction coordinate and through the intrinsic reaction coordinate (IRC) analysis[103, 104] to ensure a connection between the identified TS, reactants, and products. Zero-point vibrational energy, entropy, and temperature

corrections were determined at 553.15 K and 1 atm (experimental reaction conditions[62]) using the Shermo program[105] and the quasi-rigid rotor harmonic oscillator (qRRHO) approximation. Low frequencies were raised to 100 cm^{-1} to account for the breakdown of the harmonic approximation for low-lying vibrational modes.[106] Translational and rotational degrees of freedom were removed for chemisorbed species. The natural bond orbital analysis (NBO)[107, 108] was performed using the NBO7 program[109] via ORCA interface. The ma-def2-TZVP basis set was employed. NBO provided visual representation of bonding between metal and ligands and insights into the stability of TS complexes using the second-order perturbation theory analysis of the Fock matrix. Orbital visualizations were generated using the built-in orca_plot feature and Chemcraft software.[110]

The energetic span model[111] was applied to DFT-computed energy profiles of explored catalytic cycles to assess feasibility of proposed reaction mechanisms. The model assumes that the rate of the overall reaction is determined by one TS and one reaction intermediate. The computed energetic spans are compared to the span of 1.34 eV estimated from the experimentally measured turnover frequency (Section S2).

3. Results and discussion

We began this study by examining reaction energetics of two hypothetical reaction mechanisms that may occur on the $OReO_3$ sites: the direct mechanism proposed by Qi et al.[89] and the ketene mechanism inspired by a study by Cai et al. of DME carbonylation on a heteropolyacid catalyst.[112] In the direct mechanism, no stable reaction intermediate could have been located (Section S3.1). In the ketene mechanism (Section S3.2), the lowest estimate of the energetic span based on thermodynamics alone (1.99 eV) was already too high in comparison with the value derived from experiment (1.34 eV). Thus, we can conclude that neither of the two previously proposed reaction mechanisms are likely on the $OReO_3$ sites, and other mechanistic possibilities need to be explored. In the next section, we present direct and indirect evidence suggesting in situ reduction of the $OReO_3$ species as a prerequisite for the catalytic activity.

a. Activation of the catalytic site through reduction

The reduced $OReO_x$ motifs are the most likely catalytic site candidates for methanol carbonylation. On the one hand, both our calculations and earlier experiments[113, 114] indicate that Re(VII) sites cannot bind CO, and thus the pristine $OReO_3$ motifs are likely inert for carbonylation. On the other hand, the CO probe molecule FTIR spectrum of CO-reduced Rh/SiO_2 (Figure 8a of ref. [89]) is affected by addition of ReO_x, implying either Re-CO or Re-Rh interactions, which can only occur on the reduced ReO_x. Partial removal of =O ligands under carbonylation conditions is corroborated by the slight reduction of the Re-O EXAFS peak (Figure 6c of ref. [89]).

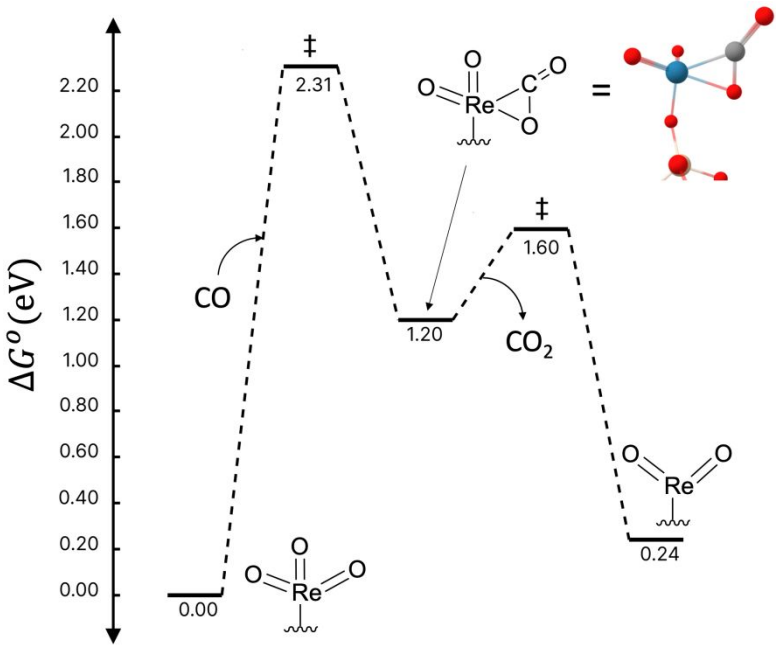

Figure 2. Gibbs free energy diagram of Re^{+7} reduction by CO to form Re^{+5} and CO_2 at 553 K and 1 bar. Red = O, yellow = Si, grey = C, and blue = Re. The high barrier for CO binding can be decomposed into the electronic component (~1.3 eV) and the entropic and temperature effects (~1 eV).

The proposed reduced $OReO_x$ catalytic sites can be generated through the synergistic action of MeOH, CO, and possibly adventitious organics. Although CO is a common reducing agent for extracting lattice O* from metal oxide surfaces,[115] we find that CO alone is unable to react with $OReO_3$. In Figure 2, a free energy diagram is reported for $OReO_3$ reduction by CO. Although the overall reaction energetics is only slightly endergonic (+0.2 eV) and thus thermodynamically favorable, the kinetic barrier for the CO binding step is prohibitively high (2.3 eV). The barrier would translate to the reduction of only 0.005% of Re sites after 1 hour under reaction conditions, according to the Eyring transition state theory. However, such sluggish $OReO_3$ reduction kinetics would be inconsistent with the lack of an induction period in the experiment and the observed steady conversion and selectivity profiles over a 60-hour period.[89] Furthermore, the computationally predicted inertness of $OReO_3$ toward CO is in line with an experimental fact that the reduction of Re_2O_7 or perrhenates by CO is very difficult and, in fact, requires prolonged harsh reaction conditions (220-485 bar of CO, 230-290°C, 48 hours) and a copper catalyst.[116] Thus, we conclude that the $OReO_3$ reduction solely by CO does not occur during MeOH carbonylation.

The presented computational and experimental arguments appear in variance with FTIR spectroscopy data of adsorbed CO on Re_2O_7/Al_2O_3 by Daniell et al,[113] where weak IR peaks of 2130 and 2080 cm^{-1} due to CO bound to the reduced ReO_x motifs appear after pretreatment in CO at very mild conditions (60°C for 1 h). Similar results would likely hold for ReO_x/SiO_2 (and thus for ReO_x/SBA-15 studied in this work), which is more reducible than ReO_x/Al_2O_3.[117] We hypothesize that the rather unexpected appearance of the reduced ReO_x at low temperatures may be caused by the effect of impurities. High-surface-area catalytic materials easily adsorb organics from a laboratory environment, especially acetone in a polymerized form.[117] The amount of such adventitious carbon can be quite large, with the carbon:metal ratio reported to

reach 1:10[118] and possibly even greater for ultradispersed catalysts. The amount of organic impurities appears to be barely affected by the catalyst calcination temperature, and their complete removal requires calcination above 750°C,[118] much higher than 450°C used in the synthesis of ReO_x/SBA-15[89] or 550 °C during preparation of Re_2O_7/Al_2O_3 (*vide supra*).[113] Since Re(VII) was reported to be reduced by alkenes at ambient temperatures and subatmospheric pressures,[114] it seems plausible that the deposited organics can also act as a reductant for $OReO_3$ motifs at rather mild reaction conditions. Once the initial fraction of reduced Re is formed, the subsequent reduction can proceed autocatalytically.[117, 119] Iron impurities present in SBA-15 (~0.05%[120]) are unlikely to promote the $OReO_3$ reduction, since iron is known to make ReO_x less reducible.[121]

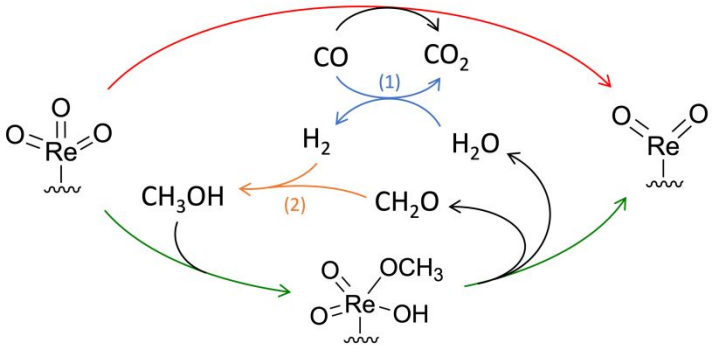

Scheme 1. A proposed pathway for Re (VII) reduction by MeOH. (1) Water-gas shift (WGS) reaction, (2) Hydrogenation of formaldehyde.

Besides organic impurities, MeOH can act as a reductant for the $OReO_3$ sites. Experimental evidence indicates that the Re(VII) to Re(V) reduction by alcohols is an elementary step in the Re-catalyzed alcohol deoxydehydration.[122] In addition, the Re(VII) reduction step is needed to explain the production of dimethoxymethane (DMM)[123] along with formaldehyde (FA)[124] during MeOH oxidation by O_2 on a Re_2O_7 catalyst. The rate-limiting steps (RLS) of Re(VII) reduction by MeOH and MeOH oxidation are likely shared, as the latter is limited by C-H bond activation in MeOH.[125] The corresponding apparent activation barrier is 21.7 kcal/mol,[125] much lower than the barrier for MeOH carbonylation (32.7 kcal/mol[89]). Neglecting entropic effects, it would correspond to reduction rates on the order of 10^5 s^{-1}. Thus, the in situ reduction of $OReO_3$ sites by MeOH during carbonylation is expected to be very rapid.

To determine the thermodynamic feasibility of $OReO_3$ reduction by MeOH, we computed Gibbs free energies (ΔG) of reactions MeOH+$OReO_3$=FA+$OReO_2$+H_2O and 3MeOH+$OReO_3$=DMM+2H_2O+$OReO_2$ with DFT at experimental MeOH carbonylation conditions. The free energies were found to be +0.95 and +1.13 eV, respectively. Although the reactions are too endergonic to generate appreciable amounts of $OReO_2$, as the associated reaction barriers are likely high, thermodynamics becomes more favorable when the reactions of FA and H_2O are taken into account (Scheme 1). First, H_2O can react with the abundant CO before desorption, as the supported Re(VII) displays notable activity in the water-gas shift (WGS) reaction CO+H_2O=CO_2+H_2 at the typical MeOH carbonylation conditions,[126] with ΔG of the WGS reaction of about -0.18 eV.[127] Second, the formed FA can be hydrogenated back to the more thermodynamically stable MeOH by WGS-generated H_2 (likely in a ReO_x-bound state), since ReO_x can catalyze hydrogenation of carbonyl compounds.[128] As both WGS and hydrogenation are expected to be quite rapid, the overall established thermodynamic equilibrium would correspond to the process $OReO_3$+CO=$OReO_2$+CO_2 with $\Delta G = 0.2$ eV (Figure 2). In this mechanistic scenario, MeOH would effectively act as a promoter to bypass the unfavorable direct CO binding step, and the net reduction would be formally driven by CO. Although the equilibrium would be shifted to the right due to negligible CO_2 pressures, the number of reduced sites is likely small due to kinetic limitations, based on the EXAFS spectra[89] and the fraction of reduced ReO_x sites formed during alkene metathesis.[129, 130]

It should be noted that H_2 formed in the WGS reaction may further react with $OReO_2$, at least in principle, reducing it all the way to Re(0) in an autocatalytic process,[117] since the temperature of a temperature-programmed reduction (TPR) peak (310°C),[83] typically associated with Re(0) formation,[117] is rather close to the MeOH carbonylation temperature (280°C). The overall conclusion can be made that during MeOH carbonylation, the reduction of Re(VII) sites does occur. Such sites likely exhibit a range of Re oxidation states, and each one of them can be a potential catalytic active site candidate. In the following sections, we will investigate Re(V) and Re(III) oxidation states in detail and study the effect of different ligand environments on energetics of three key reaction steps in carbonylation: **(1)** C-O cleavage in MeOH to form bound methyl and hydroxyl, **(2)** C-C coupling of methyl and carbonyl to form acetyl (-$COCH_3$), and **(3)** C-O bond formation between acetyl and hydroxyl to generate AA.

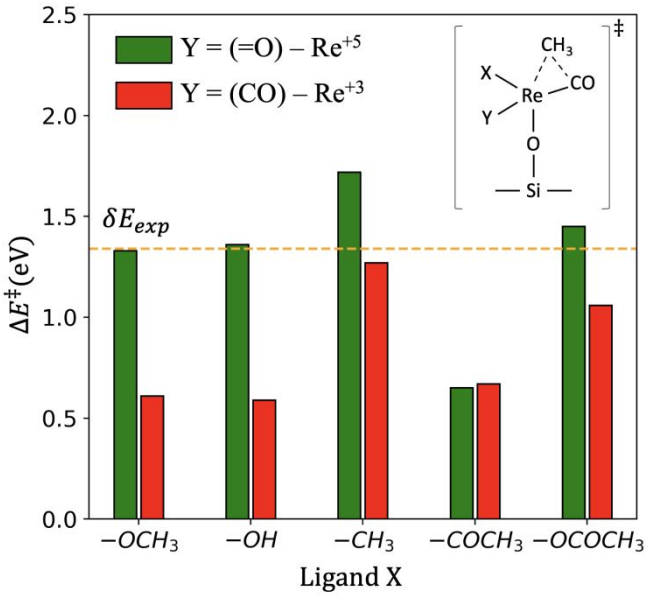

Figure 3. Electronic energy barriers of the C-C coupling of methyl and carbonyl on Re sites for various spectator ligands X and Y. The energetic span derived from experimental rate δE_{exp} is used as a heuristic metric to assess the feasibility of C-C coupling step of different complexes.

b. The C-C coupling step to form -$COCH_3$

We first focus on the C-C coupling of -CH_3 and -CO (migratory insertion) as it is the most critical step for C_2 selectivity. It is also known to be the rate-limiting step of the Cativa cycle.[131] Our initial investigations ruled out two C-C coupling mechanisms: C-C coupling through -OCO bidentate species (Section S4) and the direct C-C coupling from the gas-phase CO (Section S5). Thus, the most probable C-C coupling scenario entails methyl and carbonyl ligand coupling when both ligands are coordinated to the same Re center, akin to the migratory insertion in the Cativa process. To test this hypothesis, we modeled a representative complex containing both ligands (–CH_3 and –CO) along with an –OH group to maintain the stoichiometry of the overall reaction: $CH_3OH + CO \rightarrow CH_3COOH$. Only one oxo ligand (=O) was included (corresponding to the Re(V) state before the reaction), as two oxo ligands in $ORe(=O)_2(CH_3)(OH)(CO)$ caused CO to dissociate from the metal center. The calculated electronic barrier for the reaction $Re(=O)(CH_3)(CO)(OH) \rightarrow Re(=O)(COCH_3)(OH)$ was found to be 1.36 eV (1.56 eV free energy barrier). Although the value is comparable with the experimentally determined energy span δE_{exp} (1.34 eV; Section 2b), if taking the DFT error into account, the constructed catalytic cycle involving this intermediate (Figure S7) shows too high energetic span (2.58 eV) due to high-lying TS for the C-O bond scission. This finding prompted us to carry out the systematic screening of ligand environments modulating barriers and thermochemistry of individual reactions[132-134] to search for ligand combinations that would minimize the energetic span.

We carried out investigations of the 5-coordinate Re^{3+} and Re^{5+} complexes with the general formula $ORe(CH_3)(CO)(X)(Y)$, where X ∈ {-OCH_3, -CH_3, -OH, -$COCH_3$, -$OCOCH_3$} and Y ∈ {=O, -CO}, with the electronic reaction barriers reported in Figure 3. For Re^{5+} with Y = (=O), the barriers rank in the following order of X ligands: (-$COCH_3$) < (-OCH_3) ≈ (-OH) < (-$OCOCH_3$) < (-CH_3). All complexes, except those containing geminal -CH_3, exhibit barriers close to or below the experimental energetic span within the DFT error. Notably, substituting the oxo with the carbonyl ligand in Y (the Re^{+5} → Re^{+3} state change) consistently lowers the reaction barriers while retaining their ranking with respect to the X ligand. It was also found that removing the Y ligand leads to an unstable C-C coupling product $ORe(COCH_3)(X)$ due to the coordination number of the metal center becoming too low (3). We conclude that C–C coupling is feasible when -CH_3 and -CO are co-bound to either Re^{3+} or Re^{5+} for quite diverse 5-coordinate ligand environments.

To elucidate the role of Y ligands (–CO or =O) in the TS stabilization, NBO analysis was conducted for all TS structures (Table S3). It is revealed that the Re^{3+} center possesses two lone electron pairs across all X ligands. Second-order perturbative energy analysis indicates that one lone pair with the higher E(2) value mixes with antibonding natural orbitals associated with the Re--CH_3—CO motif where the reaction occurs, exhibiting low occupancy < 1.75 (Figure 4a and Table S3). This lone pair plays a key role in stabilizing Re^{+3} transition states through delocalization[135] and corroborating the low C-C coupling barriers for Y = (-CO) in Figure 3. The second lone pair couples with the antibonding orbital of the C–O bond through a π back-bonding interaction[136] (Figure 4b), forming a dative bond between the spectator CO ligand (ligand Y) and the metal center.

In contrast, the Re^{5+} center only possesses one lone electron pair in the TS configuration due to the presence of a Re ≡ O triple bond,[137-139] in which two of Re electrons form one σ and one π bond, and a pair of electrons from O mixes with an empty d orbital to form the third bond. The lone pair on Re is highly localized, as indicated by its high occupancy (Table S3). It does not couple significantly to C-C antibonding orbitals, resulting in a higher barrier for Y = (=O).

The effect of the Re-localized electron density on stabilizing the TS corroborates the C-C coupling reactivity trend observed in Figure 3. The -OH and -OCH_3 ligands exhibit a stronger positive mesomeric (+M) effect than $OCOCH_3$ and thereby effectively increase electron density on Re, available for mixing with the antibonding states of the CH_3--CO fragment. The -CH_3 ligand, in turn, does not induce the same effect due to the absence of a lone electron pair, resulting in the highest C-C coupling barrier. The -$COCH_3$ ligand is a notable exception – despite the -M effect that would reduce Re electron density, the C-C formation barrier is lowest among all tested ligands. We attribute the beneficial effect of the acetyl ligand to the weakening of the Re-CH_3 bond. Acetyl forms a resonance structure CH_3-C(-O^-)=Re that would increase the Re-$COCH_3$ bond order at the expense of bond orders of other single bonds, such as Re-CH_3. This, in turn, should reduce energy penalty for stretching the Re-C bond to the transition state. Consistent with this explanation, the Re-CH_3 bond lengths for X=OH/$COCH_3$ in Re(III) and Re(V) complexes are 2.11/2.13 Å and 2.08/2.12 Å, respectively, with evident elongation in complexes containing an acetyl ligand.

We conclude that the C-C coupling is more favored on Re^{3+} due to the lone pair-induced TS stabilization, particularly for X=$COCH_3$, where the low barrier is associated with weakening of the Re-CH_3 bond. However, the importance of the stabilization mechanism in the experimental system remains obscure, as the Re^{5+} sites without such stabilization exhibit barriers for four out of five tested X ligands that are low enough to be consistent with the experimental MeOH carbonylation kinetics.

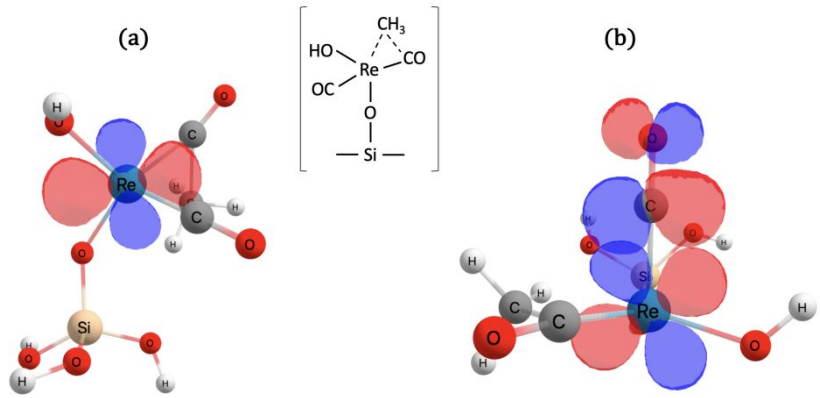

Figure 4. Natural orbitals of two lone pairs of Re in the C-C coupling TS of Re(CO)(CH_3)(CO)(OH) (Re^{+3}): (a) Orbital of lone pair 1 with low occupancy of 1.13 (max = 2) due to delocalization that stabilizes the TS complex, (b) Orbital of lone pair 2 overlaps with the π^* orbital of CO in the π back-bonding configuration. Red = O, white = H, yellow = Si, grey = C, and blue = Re. Iso-surface value = 0.08.

c. The C-O bond cleavage in MeOH

Since the favorable C-C coupling step involves the Re-coordinated methyl as a reactant, the C-O scission step in MeOH must precede it. In the Introduction, we argued that the promoter-free MeOH carbonylation activity of certain oxides, including ReO_x/SiO_2, may be associated with high oxophilicity of their reduced forms, favoring the direct C-O bond cleavage. In this section, we test this hypothesis using DFT and NBO analysis.

The two possible precursors for the -CH_3 species are CH_3OH and -OCH_3. Our calculations indicate that, upon adsorption onto the Re site, CH_3OH undergoes rapid exergonic O-H scission and converts to methoxy (Table S4).[47, 140, 141] Consequently, we restricted our investigation of the C-O scission to methoxy species and screened complexes of the form ORe(OCH_3)(X)(Y), where X ∈ {-OCH_3, -CH_3, -OH, -$COCH_3$, -$OCOCH_3$} and Y ∈ {=O, -CO, vacant}.

Figure 5 illustrates the electronic C-O scission barriers for 15 different coordination environments, encompassing both Re^{+5} and Re^{+3} oxidation states. In the high oxidation state (Y = (=O)), the barriers increase in the following order of X ligands: (-OH) ≈ (-OCH_3) < (-CH_3) < (-$OCOCH_3$) < (-$COCH_3$). Three cases with X = -OCH_3, -OH, and -CH_3 exhibit activation energies comparable to δE_{exp} (1.34 eV), whereas the barriers for X = -$COCH_3$ and -$OCOCH_3$ are significantly larger than δE_{exp}. Unexpectedly, reducing the Re oxidation state to +3, achieved by substituting the =O ligand with a -CO ligand, markedly elevates the intrinsic barrier for the C–O bond cleavage, rendering the entire set of ORe(OCH_3)(X)(CO) complexes completely inactive for C-O scission. We conclude that favorable C-O bond cleavage in methoxy is associated with Re^{+5} sites, and =O substitution by -CO has a strong inhibiting effect on the reaction.

The NBO analysis reveals that the high C-O barriers on Re^{+3} are caused by competition between O-CH_3 and C-O antibonding orbitals for the metal-localized lone electron pair. In both high and low oxidation state complexes (with and without oxo ligands), the Re center possesses only one lone electron pair, since the second pair is either absent (in Re^{+5}) or is used in forming the Re-O triple bond as the reaction progresses (in Re^{+3}). In the Re^{+5} case, the lone pair delocalizes into the antibonding orbital of the O–CH_3 bond,

weakening the bond and facilitating cleavage, thereby stabilizing the TS complex (Figure 5b and Table S5). Conversely, in the Re^{3+} case containing a CO ligand, the lone pair delocalizes into either the C–O of the CO spectator ligand or the Re–C antibonding orbital for back-donation between the CO and Re center. This back-bonding phenomenon impedes the metal's lone pair from participating in the stabilization of the TS and thus activating the C–O bond in the methoxy intermediate.

The reaction barriers for Re^{+5} (Figure 5) correlate with the mesomeric character of the X ligand. The -OH and $-OCH_3$ ligands with the greatest +M effect make the Re site electron-rich and favor electron donation to the antibonding orbital of the O--CH_3 fragment. On the other end, $-COCH_3$ with the greatest -M effect renders Re electron-poor with less TS stabilization, resulting in the highest C-O scission barrier. Similar to the effect described above in the context of the C-C coupling step, acetyl is expected to weaken single bonds, such as CH_3O-Re, which would, in turn, strengthen the CH_3-O bond and increase the C-O bond activation barrier. Although the C-O and C-C barrier trends with respect to +M ligands are similar, along with the stabilization mechanism involving a lone electron pair, the -M acetyl has an opposite effect on the C-C and C-O reaction barriers.

The C-O scission barriers on Re^{+3} have a markedly different trend. Since the lone electron pair does not participate in the coupling with the antibonding orbital, the mesomeric effect appears negligible, and the

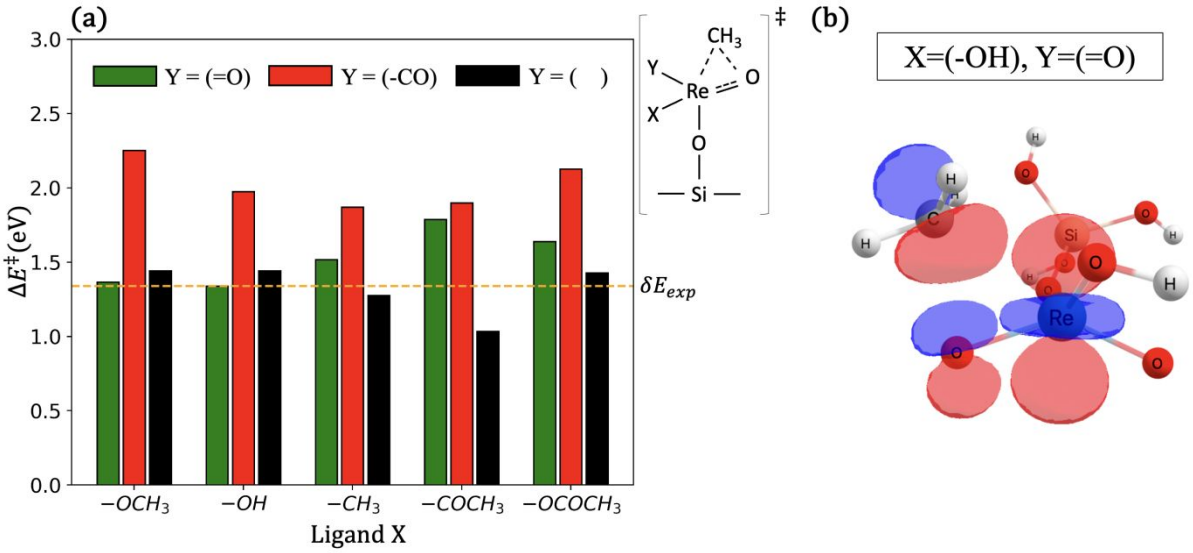

Figure 5. (a) Electronic energy barriers for the C-O cleavage step in methoxy across combinations of spectator ligands. The experimental rate-derived energy span δE_{exp} serves as a heuristic metric to assess the feasibility of the C-O scission in different complexes. (b) Natural orbital of a lone electron pair on Re overlaps with the C-O antibonding natural orbital in the TS of Re(=O)(OCH_3)(OH). Red = O, white = H, yellow = Si, grey = C, and blue = Re. Iso-surface value = 0.08 was used.

reactivity trend is determined by the electronegativity of atoms within the ligand. In particular, ligands bound to Re through O (-OH, OCH_3, $OCOCH_3$) tend to exhibit higher barriers than ligands bound through less electronegative carbon (-CH_3, $COCH_3$), presumably because of the stronger electron-withdrawing effect.

For Y = vacant, the resulting ORe(OCH_3)(X) complexes are under-coordinated and unstable, favoring the triplet ground states as observed for all X ligands except X = –$COCH_3$ (Table S6). This is in contrast with the singlet states in ORe(OCH_3)(X)(Y), where Y ∈ {=O, -CO}. The low stability of ORe(OCH_3)(X)

is manifested in too negative CO chemisorption free energies (below –1 eV; Table S7), indicating irreversible coordination with CO under experimental conditions. As a 5d transition metal, Re has nine valence orbitals available for bonding (one 6s, three 5p, and five 5d orbitals), making 3-coordinated complexes inherently unstable due to the incomplete utilization of these orbitals. Figure 5 shows that the reaction barriers for $ORe(OCH_3)(X)$ complexes (i.e. Y = vacant) are comparable to those for $ORe(=O)(OCH_3)(X)$ complexes (i.e. Y = (=O)) in all cases except X = $–COCH_3$. However, NBO analysis reveals that, unlike the Y = (=O) case, there is no lone electron pair delocalizing to the antibonding orbital of the $O–CH_3$ bond (Table S8). We attribute the low reaction barriers to the bond order conservation principle. Carbonyl contributes the Re=C=O resonance structure that increases the Re-CO bond order and reduces bond orders for all other single bonds – in this regard, carbonyl resembles acetyl. Thus, upon CO removal, the $Re\text{-}OCH_3$ bond becomes stronger, in turn weakening the $O\text{-}CH_3$ bond and facilitating its cleavage. Since the newly formed $Re\text{-}CH_3$ bond becomes too strong, an ultra-stable product is produced that forms a thermodynamic sink – an issue that will be discussed in Section 3e.

d. C-O bond formation

Once the acetyl species $-COCH_3$ is formed in the favorable C-C formation step (Section 3b), the C-O bond formation occurs, leading to the final product. AA can be produced either directly through $-COCH_3$ and -OH or indirectly through $-COCH_3$ and =O, followed by the O-H bond formation. To determine the kinetically favored C-O bond formation, we identified 36 distinct transition states and calculated the corresponding activation barriers. Figure 6 depicts the distribution of activation barriers for acetate-mediated and direct AA formation. The direct AA formation exhibits lower barriers, with an average of 1.11 eV, whereas the average electronic barrier for acetate formation is 1.77 eV. Notably, 18 out of 24 acetate formation TS exhibit barriers much larger than δE_{exp} (Table S9). In contrast, of the 13 TSs modeled

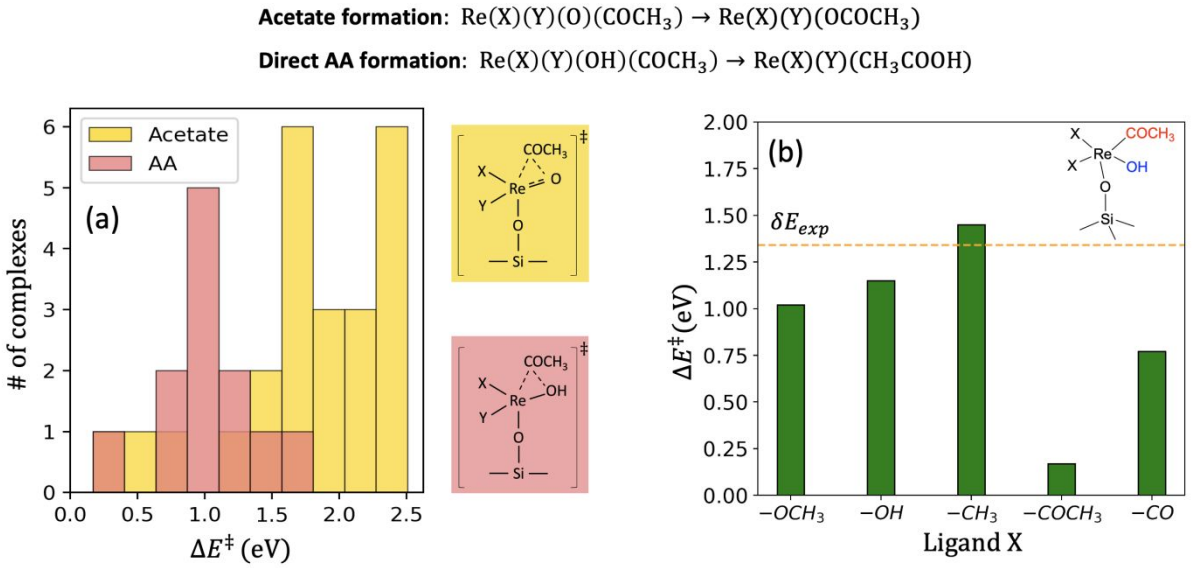

Figure 6. (a) Histogram of electronic energy barriers for the C-O bond formation. A total of 36 TS complexes were identified, associated with two different products (24 values for acetate ligand and 12 values for AA ligand). Individual data points are included in Table S9, S10. (b) Influence of the spectator ligands on the electronic TS barriers of the direct AA formation. Experimental rate-derived energy span δE_{exp} is shown as the heuristic metric to evaluate the feasibility of the C-O bond formation across different complexes.

for the direct AA formation, only 3 have barriers exceed δE_{exp} (Table S10). Overall, the direct formation of AA from acetyl and hydroxyl is kinetically favored.

Focusing on the direct AA formation from -$COCH_3$ and -OH, we investigated the reactivity trend of the C-O bond formation by examining the complexes with the formula ORe($COCH_3$)(OH)(X)(X), where X ∈ {-OCH_3, -CH_3, -OH, -$COCH_3$, -CO}. Figure 6b shows that the C-O bond formation barriers increase in the order (-$COCH_3$) < (-CO) < (-OCH_3) < (-OH) < (-CH_3) and thus parallel the trend we observed for the C-C coupling, suggesting a similar activation mechanism. The lower activation energies for -$COCH_3$ and -CO suggest that the C-O bond formation is favored by π-acceptor over σ/π-donor ligands (-OCH_3, -OH, -CH_3). NBO analysis (Table S11) reveals that the natural orbitals of Re lone pair(s) in the cases with X = CO or –$COCH_3$ exhibit low occupancy (1.644 and 1.531 respectively), indicating that these lone pairs delocalize. Second-order perturbation theory analysis shows that these lone pairs contribute to the antibonding orbitals of the C–O bond in the carbonyl groups of both -CO and -$COCH_3$, indicating that they primarily engage in back-bonding, thereby strengthening the Re–CO bond. The lone-pair delocalization decreases electron density of the metal center, weakening bonds between metal and the reactive ligands -$COCH_3$ and -OH as indicated by the low occupancy of Re-$COCH_3$ natural bonding orbital for both cases X =-$COCH_3$ and -CO (1.912 and 1.865 respectively) and the low occupancy of the Re-OH natural bonding orbital for X = -CO (1.934) (Table S12). In contrast, for X = OH, OCH_3, and CH_3, the single lone pair of Re remains localized around the Re center (lone-pair orbital occupancy > 1.9, Table S11), resulting in an electron-rich Re center, which strengthens the Re-$COCH_3$ and Re-OH bond (high occupancy of natural bonding orbitals) and hinders C–O bond formation. Consequently, the barriers of these σ/π-donor ligand complexes are larger than the complexes with π-acceptor spectator ligands. The observed behavior is typical for reductive elimination reactions, promoted by high-coordination, electron-poor metal centers.[136, 142-144]

e. Dilemma of the low- vs. high-oxidation state Re center for serial C-O scission and C-C formation

Our computational data indicate that for all three key elementary steps – C-O scission, C-C bond formation, and C-O bond formation – low reaction barriers can be obtained, consistent with the experimental energetic span of 1.34 eV. Although individual reaction steps are feasible, combining them in a catalytic cycle requires overcoming several contradictions in order to reconcile calculations and experiment. For example, according to Figure 3, the C-C bond formation step is most feasible on Re(III) sites, where the Y = (=O) ligand is replaced with Y = (-CO), as CO destabilizes the reacting CO and lowers the C-C coupling barrier. However, this would require C-O scission to occur on Re(I). By analogy with pentacarbonyl rhenium hydride $HRe(CO)_5$, the silica-bound Re(I) would be highly coordinated to CO, which would deactivate the site toward C-O scission, according to Figure 5. Indeed, our calculations indicate C-O scission barriers on Re(I) to be exceptionally high (Figure S6). Additionally, MeOH adsorption would require CO desorption to free up sites for bonding, which would result in negative reaction orders with respect to CO, contradicting experimental evidence.[89] We can conclude that, despite highly favorable C-C coupling, Re(III) sites (or Re(I) prior to oxidation by MeOH) are unlikely to be involved in this reaction step.

The arguments above imply that the C-C coupling likely occurs on Re(V) sites, perhaps with Y= (-$COCH_3$), (-OH), or (-OCH_3), which all show barriers lower or reasonably close to the experimental energetic span (Figure 4). However, the preceding C-O bond activation in MeOH on Re(III) is difficult to accomplish, as the CO ligand, likely to be present due to its high binding affinity (Table S7), withdraws electron density and thereby deactivates the complex (Figure 5). Even in the case of no CO binding to the Re(III) complexes (-Re(OCH_3)(X)), when the barriers are low, the metal center is under-coordinated, and

the reactant state is unstable. Therefore, products of the C-O bond cleavage would exhibit exceptional stability compared to their corresponding reactants, as indicated by very negative electronic reaction energies across all tested complexes (Figure 7). High product stability creates a thermodynamic sink in the energy profile, translating to a large energetic span, as a representative example reveals in Section S7. In turn, more favorable C-O scission on Re(V) would result in Re(VII) that cannot bind CO at all (Section S3, S4, and S5) and thus cannot catalyze the C-C formation. We conclude that monopodal rhenium sites with typical ligand environments cannot simultaneously catalyze C-O cleavage and C-C coupling/C-O formation reactions.

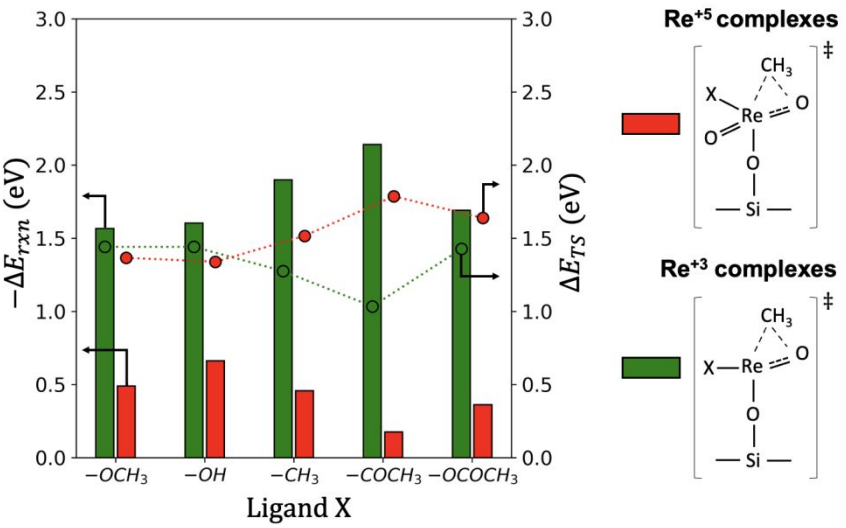

Figure 7. Electronic reaction energies (bars) and electronic barriers (circles) of the C-O bond cleavage with oxo ligand (Re^{+5}) and without oxo ligand (Re^{+3}) for different ligands X.

One possibility for reconciling C-O cleavage and C-C coupling steps entails catalysis by multinuclear complexes. Although the monopodal $OReO_3$ sites were initially corroborated by EXAFS,[62] a subsequent study by Finzel et al. highlighted limitations of the experimental methodology for characterizing this system.[70] Consistent with this possibility, experimental studies of ReO_x/SiO_2 and Rh-ReO_x/SiO_2 catalysts have demonstrated significant alterations in rhenium coordination in the presence of reducing agents such as H_2 and CO[145-148]. Multinuclear Re complexes would allow C-O bond cleavage and C-C coupling to occur at distinct centers, offering a potential solution to the methanol carbonylation mechanism on ReO_x/SiO_2.

4. Conclusion

In this study, we have conducted a detailed quantum-mechanical investigation into the methanol carbonylation reaction to form acetic acid on a silica-supported single-site $OReO_3/SiO_2$ catalyst. Our findings reveal that the activation of the -$OReO_3$ catalytic site through reduction is a crucial step for initiating the carbonylation process. Through density functional theory (DFT) calculations, natural bond orbital (NBO) analysis, and the energetic span model, we have elucidated the reactivity trends of surface species in various coordination environments. Our analysis indicates that the C–C coupling step, essential for acetic acid formation, is kinetically favorable in both Re(V) and Re(III) complexes, with Re(III) being preferred due to transition state stabilization by a metal-localized lone electron pair. However, the preceding C–O bond activation step, which is favorable on Re(V), leads to an inactive Re(VII) complex, posing a significant challenge for the overall catalytic cycle. The C–O bond activation on Re(III), while compatible with subsequent C–C bond formation, exhibits a high barrier due to the electron-withdrawing nature of the CO ligand. These findings suggest that the high methanol carbonylation activity observed on the ReO_x/SiO_2 catalyst cannot be fully explained by monopodal catalytic sites alone. Instead, our results highlight the potential involvement of multinuclear sites or more exotic ligand environments that facilitate a cooperative reaction mechanism.

Acknowledgements

The authors thank Stephen Garofalini for providing the atomic structure of the vitreous silica. The authors acknowledge the ACS Petroleum Research Fund Doctoral New Investigator Award 65292-DNI5 for the financial support. This work used SDSC Expanse CPU at the University of California San Diego through allocation CHM230055 from the Advanced Cyberinfrastructure Coordination Ecosystem: Services & Support (ACCESS) program, which is supported by National Science Foundation grants #2138259, #2138286, #2138307, #2137603, and #2138296.

References

(1) Intelligence, M. *Acetic Acid - Market Share Analysis, Industry Trends & Statistics, Growth Forecasts 2019 - 2029*; 2024. https://www.researchandmarkets.com/reports/4520125/acetic-acid-market-share-analysis-industry.
(2) Kalck, P.; Le Berre, C.; Serp, P. Recent advances in the methanol carbonylation reaction into acetic acid. *Coordination Chemistry Reviews* **2020**, *402*, 213078. DOI: 10.1016/j.ccr.2019.213078 (acccessed 2023/02/15/22:27:41). From DOI.org (Crossref).
(3) Jones, J. H. The Cativa™ process for the manufacture of acetic acid. *Platinum Metals Review* **2000**, *44* (3), 94-105.
(4) Garland, C. S.; Giles, M. F.; Poole, A. D.; Sunley, J. G. Process for the production of a carboxylic acid. Google Patents: 1996.
(5) Ghaffar, T.; Adams, H.; Maitlis, P. M.; Haynes, A.; Sunley, G. J.; Baker, M. J. Spectroscopic identification and reactivity of [Ir (CO) 3 I 2 Me], a key reactive intermediate in iridium catalysed methanol carbonylation. *Chemical Communications* **1998**, (9), 1023-1024.
(6) Haynes, A. Acetic acid synthesis by catalytic carbonylation of methanol. *Catalytic carbonylation reactions* **2006**, 179-205.
(7) Forster, D. On the mechanism of a rhodium-complex-catalyzed carbonylation of methanol to acetic acid. *Journal of the American Chemical Society* **1976**, *98* (3), 846-848. DOI: 10.1021/ja00419a041 (acccessed 2023/02/15/22:30:41). From DOI.org (Crossref).
(8) Paulik, F. E.; Roth, J. F. Novel catalysts for the low-pressure carbonylation of methanol to acetic acid. *Chemical Communications (London)* **1968**, (24), 1578a-1578a.
(9) Roth, J. F. The Production of Acetic Acid: Rhodium catalysed carbonylation of methanol. *Platinum metals review* **1975**, *19* (1), 12-14.
(10) Forster, D. MECHANISM OF RHODIUM COMPLEX-CATALYZED CARBONYLATION OF METHANOL TO ACETIC ACID. *Annals of the New York Academy of Sciences* **1977**, *295* (1), 79-82.
(11) Forster, D. Mechanistic Pathways in the Catalytic Carbonylation of Methanol by Rhodium and Iridium Complexes. In *Advances in Organometallic Chemistry*, Vol. 17; Elsevier, 1979; pp 255-267.
(12) Forster, D.; Dekleva, T. W. Catalysis of the carbonylation of alcohols to carboxylic acids including acetic acid synthesis from methanol. *Journal of Chemical Education* **1986**, *63* (3), 204.
(13) Von Kutepow, N.; Himmele, W.; Hohenschutz, H. Die Synthese von Essigsäure aus Methanol und Kohlenoxyd. *Chemie Ingenieur Technik* **1965**, *37* (4), 383-388.
(14) Sevostyanova, N.; Batashev, S. Catalysts for Carbonylation of Alcohols to Obtain Carboxylic Acids and Esters. *Russian Journal of Applied Chemistry* **2022**, *95* (8), 1085-1106.
(15) Zoeller, J. R.; Singleton, A. H.; Tustin, G. C.; Carver, D. L. Vapor phase carbonylation process using gold catalysts. Google Patents: 2003.
(16) Zoeller, J. R.; Singleton, A. H.; Tustin, G. C.; Carver, D. L. Gold based heterogeneous carbonylation catalysts. Google Patents: 2003.
(17) Zoeller, J. R.; Singleton, A. H.; Tustin, G. C.; Carver, D. L. Method for carbonylation of lower aliphatic alcohols using tin promoted platinum catalyst. Google Patents: 2003.
(18) Ren, Z.; Lyu, Y.; Feng, S.; Song, X.; Ding, Y. A highly efficient single site Rh-POL-PPh3 catalyst for heterogeneous methanol carbonylation. *Molecular Catalysis* **2017**, *442*, 83-88. DOI: 10.1016/j.mcat.2017.09.007 (acccessed 2022/08/13/15:19:46). From DOI.org (Crossref).

(19) Feng, S.; Lin, X.; Song, X.; Mei, B.; Mu, J.; Li, J.; Liu, Y.; Jiang, Z.; Ding, Y. Constructing efficient single Rh sites on activated carbon via surface carbonyl groups for methanol carbonylation. *ACS Catalysis* **2020**, *11* (2), 682-690.
(20) Mu, J.; Long, G.; Song, X.; Feng, S.; Li, X.; Yuan, Q.; Li, B.; Jiang, Z.; Yan, L.; Ding, Y. Engineering the Coordination Environment of Single-Rh-Site with N and S Atoms for Efficient Methanol Carbonylation. *Advanced Functional Materials* **2023**, *33* (52), 2305823.
(21) Feng, S.; Lin, X.; Song, X.; Liu, Y.; Jiang, Z.; Hemberger, P.; Bodi, A.; Ding, Y. The role of H2 on the stability of the single-metal-site Ir1/AC catalyst for heterogeneous methanol carbonylation. *Journal of Catalysis* **2020**, *381*, 193-203. DOI: 10.1016/j.jcat.2019.10.032 (acccessed 2022/08/13/15:19:25). From DOI.org (Crossref).
(22) Zehl, G.; Bischoff, S.; Lücke, B. Vapor-phase carbonylation of methanol on an active carbon supported iridium-catalyst. *Catalysis letters* **1993**, *19*, 247-255.
(23) Hensley, A. J.; Zhang, J.; Vinçon, I.; Hernandez, X. P.; Tranca, D.; Seifert, G.; McEwen, J.-S.; Wang, Y. Mechanistic understanding of methanol carbonylation: Interfacing homogeneous and heterogeneous catalysis via carbon supported IrLa. *Journal of Catalysis* **2018**, *361*, 414-422.
(24) Kwak, J. H.; Dagle, R.; Tustin, G. C.; Zoeller, J. R.; Allard, L. F.; Wang, Y. Molecular active sites in heterogeneous Ir–La/C-catalyzed carbonylation of methanol to acetates. *The Journal of Physical Chemistry Letters* **2014**, *5* (3), 566-572.
(25) Feng, S.; Song, X.; Ren, Z.; Ding, Y. La-Stabilized, Single-Atom Ir/AC Catalyst for Heterogeneous Methanol Carbonylation to Methyl Acetate. *Ind. Eng. Chem. Res.* **2019**, *58* (12), 4755-4763. DOI: 10.1021/acs.iecr.8b05402 (acccessed 2023/02/15/23:09:38). From DOI.org (Crossref).
(26) Ren, Z.; Lyu, Y.; Feng, S.; Song, X.; Ding, Y. Acid-promoted Ir-La-S/AC-catalyzed methanol carbonylation on single atomic active sites. *Chinese Journal of Catalysis* **2018**, *39* (6), 1060-1069. DOI: 10.1016/S1872-2067(18)63019-0 (acccessed 2023/11/16/18:18:40). From DOI.org (Crossref).
(27) Hansen, J. B.; Joensen, F. H.; Topsoe, H. F. Process for preparing acetic acid, methyl acetate, acetic anhydride or mixtures thereof. Google Patents: 1993.
(28) Ren, Z.; Liu, Y.; Lyu, Y.; Song, X.; Zheng, C.; Feng, S.; Jiang, Z.; Ding, Y. Single-atom Rh based bipyridine framework porous organic polymer: A high active and superb stable catalyst for heterogeneous methanol carbonylation. *Journal of Catalysis* **2019**, *369*, 249-256.
(29) Ivko, S. A.; James, A. M.; Derry, M. J.; Dawson, R.; Haynes, A. Heterogenisation of a carbonylation catalyst on dispersible microporous polymer nanoparticles. *Catalysis Science & Technology* **2022**, *12* (2), 664-673.
(30) Park, K.; Lim, S.; Baik, J. H.; Kim, H.; Jung, K.-D.; Yoon, S. Exceptionally stable Rh-based molecular catalyst heterogenized on a cationically charged covalent triazine framework support for efficient methanol carbonylation. *Catalysis Science & Technology* **2018**, *8* (11), 2894-2900. DOI: 10.1039/C8CY00294K (acccessed 2023/11/16/19:20:30). From DOI.org (Crossref).
(31) Zhang, S.; Guo, C.; Qian, Q.; Yuan, G. Synthesis of acetic acid and acetic anhydride from methanol carbonylation with polymer supported rhodium catalyst. *Catalysis Communications* **2008**, *9* (5), 853-858. DOI: 10.1016/j.catcom.2007.09.010 (acccessed 2023/02/15/22:34:45). From DOI.org (Crossref).
(32) Li, F.; Chen, B.; Huang, Z.; Lu, T.; Yuan, Y.; Yuan, G. Sustainable catalysts for methanol carbonylation. *Green chemistry* **2013**, *15* (6), 1600-1607.
(33) Nam, J. S.; Kim, A. R.; Kim, D. M.; Chang, T. S.; Kim, B. S.; Bae, J. W. Novel heterogeneous Rh-incorporated graphitic-carbon nitride for liquid-phase carbonylation of methanol to acetic acid. *Catalysis Communications* **2017**, *99*, 141-145.
(34) Kim, D. M.; Kim, A. R.; Chang, T. S.; Koo, H. M.; Kim, J. K.; Han, G. Y.; Shin, C.-H.; Bae, J. W. Synergy effects of Al2O3 promoter on a highly ordered mesoporous heterogeneous Rh-g-C3N4 for a liquid-phase carbonylation of methanol. *Applied Catalysis A: General* **2019**, *585*, 117209.
(35) Shang, W.; Gao, M.; Chai, Y.; Wu, G.; Guan, N.; Li, L. Stabilizing Isolated Rhodium Cations by MFI Zeolite for Heterogeneous Methanol Carbonylation. *ACS Catalysis* **2021**, *11* (12), 7249-7256. DOI: 10.1021/acscatal.1c00950 (acccessed 2023/04/02/20:04:51). From DOI.org (Crossref).

(36) Newman, A. D.; Wang, Y.; Orr, S. A.; Wilson, K.; Lee, A. F. Rhodium promoted heteropolyacid catalysts for low temperature methanol carbonylation. *Catalysis Science & Technology* **2022**, *12* (12), 3886-3897.
(37) Volkova, G.; Plyasova, L.; Salanov, A.; Kustova, G.; Yurieva, T.; Likholobov, V. Heterogeneous catalysts for halide-free carbonylation of dimethyl ether. *Catalysis letters* **2002**, *80*, 175-179.
(38) Kazantsev, M. S.; Luzgin, M. V.; Volkova, G. G.; Stepanov, A. G. Carbonylation of dimethyl ether on Rh/Cs2HPW12O40: Solid-state NMR study of the mechanism of reaction in the presence of a methyl iodide promoter. *Journal of Catalysis* **2012**, *291*, 9-16.
(39) Fujimoto, K.; Shikada, T.; Omata, K.; Tominaga, H.-o. Vapor phase carbonylation of methanol with supported nickel metal catalysts. *Ind. Eng. Chem. Prod. Res. Dev.* **1982**, *21* (3), 429-432. DOI: 10.1021/i300007a015 (acccessed 2023/02/15/22:37:07). From DOI.org (Crossref).
(40) Peng, F.; Xiao-Bao, F. Direct vapor-phase carbonylation of methanol at atmospheric pressure on activated carbon-supported NiCl2–CuCl2 catalysts. *Catalysis today* **2004**, *93*, 451-455.
(41) Kapran, A. Y.; Chedryk, V. I.; Alekseenko, L. M.; Orlyk, S. M. Carbonylation of methanol over Nickel-Copper based supported catalysts. *Catalysis Letters* **2021**, *151*, 993-1002.
(42) Qi, J.; Christopher, P. Atomically Dispersed Rh Active Sites on Oxide Supports with Controlled Acidity for Gas-Phase Halide-Free Methanol Carbonylation to Acetic Acid. *Ind. Eng. Chem. Res.* **2019**, *58* (28), 12632-12641. DOI: 10.1021/acs.iecr.9b02289 (acccessed 2023/02/15/22:34:17). From DOI.org (Crossref).
(43) Wegman, R. W. Vapour phase carbonylation of methanol or dimethyl ether with metal-ion exchanged heteropoly acid catalysts. *Journal of the Chemical Society, Chemical Communications* **1994**, (8), 947-948.
(44) Dingwall, L. D.; Lee, A. F.; Lynam, J. M.; Wilson, K.; Olivi, L.; Deeley, J. M.; Gaemers, S.; Sunley, G. J. Bifunctional organorhodium solid acid catalysts for methanol carbonylation. *ACS Catalysis* **2012**, *2* (7), 1368-1376.
(45) Kapran, A. Y.; Borysevych, V.; Alekseenko, L.; Chedryk, V.; Orlyk, S. Effect of Cerium Dioxide in NiCl 2–CuCl 2 Compositions Deposited on Activated Carbon on Their Catalytic Properties in the Vapor-Phase Carbonylation of Methanol. *Theoretical and Experimental Chemistry* **2016**, *52*, 233-239.
(46) Fang, X.; Wen, F.; Ding, X.; Liu, H.; Chen, Z.; Liu, Z.; Liu, H.; Zhu, W.; Liu, Z. Highly Selective Carbonylation of CH3Cl to Acetic Acid Catalyzed by Pyridine-Treated MOR Zeolite. *Angewandte Chemie International Edition* **2022**, *61* (31), e202203859.
(47) Bhan, A.; Iglesia, E. A link between reactivity and local structure in acid catalysis on zeolites. *Accounts of Chemical Research* **2008**, *41* (4), 559-567.
(48) Zhan, E.; Xiong, Z.; Shen, W. Dimethyl ether carbonylation over zeolites. *Journal of Energy Chemistry* **2019**, *36*, 51-63.
(49) Ni, Y.; Shi, L.; Liu, H.; Zhang, W.; Liu, Y.; Zhu, W.; Liu, Z. A green route for methanol carbonylation. *Catalysis Science & Technology* **2017**, *7* (20), 4818-4822.
(50) Cheung, P.; Bhan, A.; Sunley, G. J.; Iglesia, E. Selective carbonylation of dimethyl ether to methyl acetate catalyzed by acidic zeolites. *Angewandte Chemie* **2006**, *118* (10), 1647-1650.
(51) Wang, X.; Li, R.; Yu, C.; Zhang, L.; Xu, C.; Zhou, H. Dimethyl ether carbonylation over nanosheet-assembled hierarchical mordenite. *Microporous and Mesoporous Materials* **2019**, *274*, 227-235.
(52) Feng, X.-B.; Chen, F.; He, Z.-M.; Zhao, X.-Y.; Cao, J.-P. Comparison of Dimethyl Ether Carbonylation Performance over Some Zeolites Containing 8-Member Ring Pores. *Energy & Fuels* **2022**, *36* (23), 14341-14348.
(53) Feng, X.; Yao, J.; Li, H.; Fang, Y.; Yoneyama, Y.; Yang, G.; Tsubaki, N. A brand new zeolite catalyst for carbonylation reaction. *Chemical Communications* **2019**, *55* (8), 1048-1051.
(54) Boronat, M.; Martínez-Sánchez, C.; Law, D.; Corma, A. Enzyme-like Specificity in Zeolites: A Unique Site Position in Mordenite for Selective Carbonylation of Methanol and Dimethyl Ether with CO. *Journal of the American Chemical Society* **2008**, *130* (48), 16316-16323. DOI: 10.1021/ja805607m (acccessed 2022/05/19/20:55:36). From DOI.org (Crossref).

(55) Blasco, T.; Boronat, M.; Concepción, P.; Corma, A.; Law, D.; Vidal-Moya, J. A. Carbonylation of methanol on metal–acid zeolites: Evidence for a mechanism involving a multisite active center. *Angewandte Chemie* **2007**, *119* (21), 4012-4015.
(56) Tong, C.; Zuo, J.; Wen, D.; Chen, W.; Ye, L.; Yuan, Y. Halide-free carbonylation of methanol with H-MOR supported CuCeO x catalysts. *Front. Chem. Sci. Eng.* **2021**, 1-13.
(57) Ellis, B.; Howard, M. J.; Joyner, R. W.; Reddy, K. N.; Padley, M. B.; Smith, W. J. Heterogeneous catalysts for the direct, halide-free carbonylation of methanol. In *Studies in Surface Science and Catalysis*, Vol. 101; Elsevier, 1996; pp 771-779.
(58) Zhou, L.; Li, S.; Qi, G.; Su, Y.; Li, J.; Zheng, A.; Yi, X.; Wang, Q.; Deng, F. Methanol carbonylation over copper-modified mordenite zeolite: A solid-state NMR study. *Solid State Nuclear Magnetic Resonance* **2016**, *80*, 1-6.
(59) Nie, Q.; Zhao, G.; Shen, M.; Liu, Y.; Lu, Y. Ni-MoOx bifunctional catalyst on SiO2 for vapor halide-free methanol carbonylation: Insight into synergistic catalysis between Ni and MoOx. *Applied Catalysis A: General* **2021**, *623*, 118263. DOI: 10.1016/j.apcata.2021.118263 (acccessed 2023/09/21/19:54:44). From DOI.org (Crossref).
(60) Meng, X.; Guo, H.; Wang, Q.; Xiao, Y.; Chen, C.; Hou, B.; Li, D. Elucidating the nature and role of copper species in catalytic carbonylation of methanol to methyl acetate over copper/titania–silica mixed oxides. *Catalysis Science & Technology* **2017**, *7* (16), 3511-3523.
(61) Nie, Q.; Si, J.; Meng, C.; Lan, T.; Sun, W.; Zhao, G.; Liu, Y.; Lu, Y. Cu/Sn-β catalyst enabling the one-step synthesis of methyl acetate from methanol alone via dehydrogenation coupling. *ACS Sustainable Chemistry & Engineering* **2022**, *10* (29), 9282-9294.
(62) Qi, J.; Finzel, J.; Robatjazi, H.; Xu, M.; Hoffman, A. S.; Bare, S. R.; Pan, X.; Christopher, P. Selective Methanol Carbonylation to Acetic Acid on Heterogeneous Atomically Dispersed ReO4/SiO2Catalysts. *Journal of the American Chemical Society* **2020**, *142* (33), 14178-14189. DOI: 10.1021/jacs.0c05026.
(63) Mironenko, A. V.; Vlachos, D. G. Conjugation-driven "reverse Mars–van Krevelen"-type radical mechanism for low-temperature C–O bond activation. *Journal of the American Chemical Society* **2016**, *138* (26), 8104-8113.
(64) Mars, P.; Van Krevelen, D. W. Oxidations carried out by means of vanadium oxide catalysts. *Chemical Engineering Science* **1954**, *3*, 41-59.
(65) Prasomsri, T.; Nimmanwudipong, T.; Román-Leshkov, Y. Effective hydrodeoxygenation of biomass-derived oxygenates into unsaturated hydrocarbons by MoO 3 using low H 2 pressures. *Energy & Environmental Science* **2013**, *6* (6), 1732-1738.
(66) Mine, S.; Yamaguchi, T.; Ting, K. W.; Maeno, Z.; Siddiki, S. H.; Oshima, K.; Satokawa, S.; Shimizu, K.-i.; Toyao, T. Reverse water-gas shift reaction over Pt/MoO x/TiO 2: reverse Mars–van Krevelen mechanism via redox of supported MoO x. *Catalysis Science & Technology* **2021**, *11* (12), 4172-4180.
(67) Goulas, K. A.; Mironenko, A. V.; Jenness, G. R.; Mazal, T.; Vlachos, D. G. Fundamentals of C–O bond activation on metal oxide catalysts. *Nature Catalysis* **2019**, *2* (3), 269-276.
(68) Calafat, A.; Laine, J. Factors affecting the carbonylation of methanol over sulfided CoMo/C catalysts at atmospheric pressure. *Catalysis letters* **1994**, *28*, 69-77.
(69) Toledo, F.; Ghampson, I.; Sepúlveda, C.; García, R.; Fierro, J.; Videla, A.; Serpell, R.; Escalona, N. Effect of Re content and support in the liquid phase conversion of furfural to furfuryl alcohol and 2-methyl furan over ReOx catalysts. *Fuel* **2019**, *242*, 532-544.
(70) Finzel, J.; Sanroman Gutierrez, K. M.; Hoffman, A. S.; Resasco, J.; Christopher, P.; Bare, S. R. Limits of Detection for EXAFS Characterization of Heterogeneous Single-Atom Catalysts. *ACS Catalysis* **2023**, *13* (9), 6462-6473. DOI: 10.1021/acscatal.3c01116 (acccessed 2023/11/27/21:42:38). From DOI.org (Crossref).
(71) Garofalini, S. H. Molecular dynamics computer simulations of silica surface structure and adsorption of water molecules. *Journal of Non-Crystalline Solids* **1990**, *120* (1), 1-12. DOI: 10.1016/0022-3093(90)90184-N (acccessed 2022/02/16/18:10:57). From ScienceDirect.
(72) Misawa, M.; Price, D.; Suzuki, K. The short-range structure of alkali disilicate glasses by pulsed neutron total scattering. *Journal of Non-Crystalline Solids* **1980**, *37* (1), 85-97.

(73) Perez-Beltran, S.; Ramírez-Caballero, G. E.; Balbuena, P. B. First-principles calculations of lithiation of a hydroxylated surface of amorphous silicon dioxide. *The Journal of Physical Chemistry C* **2015**, *119* (29), 16424-16431.
(74) Grimley, D. I.; Wright, A. C.; Sinclair, R. N. Neutron scattering from vitreous silica IV. Time-of-flight diffraction. *Journal of Non-Crystalline Solids* **1990**, *119* (1), 49-64.
(75) Mozzi, R.; Warren, B. The structure of vitreous silica. *Journal of Applied Crystallography* **1969**, *2* (4), 164-172.
(76) Da Silva, J.; Pinatti, D.; Anderson, C.; Rudee, M. A refinement of the structure of vitreous silica. *The Philosophical Magazine: A Journal of Theoretical Experimental and Applied Physics* **1975**, *31* (3), 713-717.
(77) Delpuech, N.; Mazouzi, D.; Dupre, N.; Moreau, P.; Cerbelaud, M.; Bridel, J.; Badot, J.-C.; De Vito, E.; Guyomard, D.; Lestriez, B. Critical role of silicon nanoparticles surface on lithium cell electrochemical performance analyzed by FTIR, Raman, EELS, XPS, NMR, and BDS spectroscopies. *The Journal of Physical Chemistry C* **2014**, *118* (31), 17318-17331.
(78) Ewing, C. S.; Bhavsar, S.; Veser, G. t.; McCarthy, J. J.; Johnson, J. K. Accurate amorphous silica surface models from first-principles thermodynamics of surface dehydroxylation. *Langmuir* **2014**, *30* (18), 5133-5141.
(79) Shenderovich, I. G.; Buntkowsky, G.; Schreiber, A.; Gedat, E.; Sharif, S.; Albrecht, J.; Golubev, N. S.; Findenegg, G. H.; Limbach, H.-H. Pyridine-15 Na mobile NMR sensor for surface acidity and surface defects of mesoporous silica. *The Journal of Physical Chemistry B* **2003**, *107* (43), 11924-11939.
(80) Rimoldi, M.; Mezzetti, A. Site isolated complexes of late transition metals grafted on silica: challenges and chances for synthesis and catalysis. *Catalysis Science & Technology* **2014**, *4* (9), 2724-2740.
(81) Khan, S. A.; Godahewa, S. M.; Wimalasiri, P. N.; Thompson, W. H.; Scott, S. L.; Peters, B. Modeling the structural heterogeneity of vicinal silanols and its effects on TiCl4 grafting onto amorphous silica. *Chemistry of Materials* **2022**, *34* (9), 3920-3930.
(82) Fleischman, S. D.; Scott, S. L. Evidence for the pairwise disposition of grafting sites on highly dehydroxylated silicas via their reactions with Ga (CH3) 3. *Journal of the American Chemical Society* **2011**, *133* (13), 4847-4855.
(83) Vuurman, M.; Stufkens, D.; Oskam, A.; Wachs, I. Structural determination of surface rhenium oxide on various oxide supports (Al2O3, ZrO2, TiO2 and SiO2). *Journal of molecular catalysis* **1992**, *76* (1-3), 263-285.
(84) Smith Jr, W. T.; Line Jr, L. E.; Bell, W. The vapor pressures of rhenium heptoxide and perrhenic acid. *Journal of the American Chemical Society* **1952**, *74* (19), 4964-4966.
(85) Zhuravlev, L. Concentration of hydroxyl groups on the surface of amorphous silicas. *Langmuir* **1987**, *3* (3), 316-318.
(86) Scott, S. L.; Basset, J.-M. Coordination chemistry on surfaces: a new method to graft rhenium (VII) oxide on highly dehydroxylated oxides. *Journal of the American Chemical Society* **1994**, *116* (26), 12069-12070.
(87) Lee, E. L.; Wachs, I. E. In situ Raman spectroscopy of SiO2-supported transition metal oxide catalysts: an isotopic 18O− 16O exchange study. *The Journal of Physical Chemistry C* **2008**, *112* (16), 6487-6498.
(88) Lee, E. L.; Wachs, I. E. In situ spectroscopic investigation of the molecular and electronic structures of SiO2 supported surface metal oxides. *The Journal of Physical Chemistry C* **2007**, *111* (39), 14410-14425.
(89) Qi, J.; Finzel, J.; Robatjazi, H.; Xu, M.; Hoffman, A. S.; Bare, S. R.; Pan, X.; Christopher, P. Selective Methanol Carbonylation to Acetic Acid on Heterogeneous Atomically Dispersed ReO4/SiO2 Catalysts. *Journal of the American Chemical Society* **2020**, *142* (33), 14178-14189. DOI: 10.1021/jacs.0c05026 (acccessed 2022/03/02/19:28:25). From ACS Publications.
(90) Neese, F.; Wennmohs, F.; Becker, U.; Riplinger, C. The ORCA quantum chemistry program package. *The Journal of Chemical Physics* **2020**, *152* (22), 224108. DOI: 10.1063/5.0004608 (acccessed 2023/03/20/19:34:03). From DOI.org (Crossref).

(91) Zheng, J.; Xu, X.; Truhlar, D. G. Minimally augmented Karlsruhe basis sets. *Theoretical Chemistry Accounts* **2011**, *128* (3), 295-305. DOI: 10.1007/s00214-010-0846-z (acccessed 2023/10/02/15:17:37). From DOI.org (Crossref).
(92) Mardirossian, N.; Head-Gordon, M. ωB97X-V: A 10-parameter, range-separated hybrid, generalized gradient approximation density functional with nonlocal correlation, designed by a survival-of-the-fittest strategy. *Physical Chemistry Chemical Physics* **2014**, *16* (21), 9904. DOI: 10.1039/c3cp54374a (acccessed 2023/02/09/22:51:22). From DOI.org (Crossref).
(93) Grimme, S.; Antony, J.; Ehrlich, S.; Krieg, H. A consistent and accurate ab initio parametrization of density functional dispersion correction (DFT-D) for the 94 elements H-Pu. *The Journal of Chemical Physics* **2010**, *132* (15), 154104. DOI: 10.1063/1.3382344 (acccessed 2024/03/03/05:56:38). From DOI.org (Crossref).
(94) Johnson, E. R.; Becke, A. D. A post-Hartree-Fock model of intermolecular interactions: Inclusion of higher-order corrections. *The Journal of chemical physics* **2006**, *124* (17).
(95) Grimme, S.; Ehrlich, S.; Goerigk, L. Effect of the damping function in dispersion corrected density functional theory. *Journal of Computational Chemistry* **2011**, *32* (7), 1456-1465. DOI: 10.1002/jcc.21759 (acccessed 2024/04/08/21:46:52). From DOI.org (Crossref).
(96) Whitten, J. L. Coulombic potential energy integrals and approximations. *The Journal of Chemical Physics* **1973**, *58* (10), 4496-4501. DOI: 10.1063/1.1679012 (acccessed 2024/04/23/19:42:05). From DOI.org (Crossref).
(97) Kendall, R. A.; Früchtl, H. A. The impact of the resolution of the identity approximate integral method on modern ab initio algorithm development. *Theoretical Chemistry Accounts: Theory, Computation, and Modeling (Theoretica Chimica Acta)* **1997**, *97* (1-4), 158-163. DOI: 10.1007/s002140050249 (acccessed 2024/04/23/19:43:50). From DOI.org (Crossref).
(98) Eichkorn, K.; Weigend, F.; Treutler, O.; Ahlrichs, R. Auxiliary basis sets for main row atoms and transition metals and their use to approximate Coulomb potentials. *Theoretical Chemistry Accounts: Theory, Computation, and Modeling (Theoretica Chimica Acta)* **1997**, *97* (1-4), 119-124. DOI: 10.1007/s002140050244 (acccessed 2024/04/23/19:44:13). From DOI.org (Crossref).
(99) Neese, F.; Wennmohs, F.; Hansen, A.; Becker, U. Efficient, approximate and parallel Hartree–Fock and hybrid DFT calculations. A 'chain-of-spheres' algorithm for the Hartree–Fock exchange. *Chemical Physics* **2009**, *356* (1-3), 98-109. DOI: 10.1016/j.chemphys.2008.10.036 (acccessed 2024/04/23/19:49:46). From DOI.org (Crossref).
(100) Henkelman, G.; Jónsson, H. Improved tangent estimate in the nudged elastic band method for finding minimum energy paths and saddle points. *The Journal of Chemical Physics* **2000**, *113* (22), 9978-9985. DOI: 10.1063/1.1323224 (acccessed 2022/04/10/17:17:48). From DOI.org (Crossref).
(101) Henkelman, G.; Uberuaga, B. P.; Jónsson, H. A climbing image nudged elastic band method for finding saddle points and minimum energy paths. *The Journal of Chemical Physics* **2000**, *113* (22), 9901-9904. DOI: 10.1063/1.1329672 (acccessed 2022/04/10/17:17:40). From DOI.org (Crossref).
(102) Baker, J. An algorithm for the location of transition states. *Journal of Computational Chemistry* **1986**, *7* (4), 385-395.
(103) Deng, L.; Ziegler, T.; Fan, L. A combined density functional and intrinsic reaction coordinate study on the ground state energy surface of H2CO. *The Journal of chemical physics* **1993**, *99* (5), 3823-3835.
(104) Deng, L.; Ziegler, T. The determination of intrinsic reaction coordinates by density functional theory. *International Journal of Quantum Chemistry* **1994**, *52* (4), 731-765.
(105) Lu, T.; Chen, Q. Shermo: A general code for calculating molecular thermochemistry properties. *Computational and Theoretical Chemistry* **2021**, *1200*, 113249. DOI: 10.1016/j.comptc.2021.113249 (acccessed 2023/04/03/14:58:58). From DOI.org (Crossref).
(106) Ribeiro, R. F.; Marenich, A. V.; Cramer, C. J.; Truhlar, D. G. Use of Solution-Phase Vibrational Frequencies in Continuum Models for the Free Energy of Solvation. *The Journal of Physical Chemistry B* **2011**, *115* (49), 14556-14562. DOI: 10.1021/jp205508z (acccessed 2023/04/03/15:01:29). From DOI.org (Crossref).

(107) Foster, J. P.; Weinhold, F. Natural hybrid orbitals. *Journal of the American Chemical Society* **1980**, *102* (24), 7211-7218.
(108) Reed, A. E.; Weinhold, F. Natural bond orbital analysis of near-Hartree–Fock water dimer. *The Journal of chemical physics* **1983**, *78* (6), 4066-4073.
(109) *NBO 7.0. E. D. Glendening, J. K. Badenhoop, A. E. Reed, J. E. Carpenter, J. A. Bohmann, C. M. Morales, P. Karafiloglou, C. R. Landis, and F. Weinhold, Theoretical Chemistry Institute, University of Wisconsin, Madison, WI (2018)*; (accessed.
(110) *Chemcraft - graphical software for visualization of quantum chemistry computations. Version 1.8, build 682. https://www.chemcraftprog.com*; (accessed.
(111) Kozuch, S.; Shaik, S. How to Conceptualize Catalytic Cycles? The Energetic Span Model. *Accounts of Chemical Research* **2011**, *44* (2), 101-110. DOI: 10.1021/ar1000956 (acccessed 2022/11/05/13:36:44). From DOI.org (Crossref).
(112) Cai, K.; Li, Y.; Shen, H.; Cheng, Z.; Huang, S.; Wang, Y.; Ma, X. A density functional theory study on the mechanism of Dimethyl ether carbonylation over heteropolyacids catalyst. *Frontiers of Chemical Science and Engineering* **2021**, *15* (2), 319-329. DOI: 10.1007/s11705-020-1957-2 (acccessed 2024/03/30/23:40:44). From DOI.org (Crossref).
(113) Daniell, W.; Weingand, T.; Knözinger, H. Redox properties of Re2O7/Al2O3 as investigated by FTIR spectroscopy of adsorbed CO. *Journal of Molecular Catalysis A: Chemical* **2003**, *204*, 519-526.
(114) Olsthoorn, A.; Boelhouwer, C. An infrared spectroscopic study of the Re2O7Al2O3 metathesis catalyst: II. Catalytic properties. *Journal of Catalysis* **1976**, *44* (2), 207-216.
(115) Doornkamp, C.; Ponec, V. The universal character of the Mars and Van Krevelen mechanism. *Journal of Molecular Catalysis A: Chemical* **2000**, *162* (1-2), 19-32.
(116) Crocker, L. S.; Gould, G. L.; Heinekey, D. M. Improved synthesis of carbonylrhenium. *Journal of organometallic chemistry* **1988**, *342* (2), 243-244.
(117) Arnoldy, P.; Van Oers, E.; Bruinsma, O.; De Beer, V.; Moulijn, J. Temperature-programmed reduction of Al2O3-, SiO2-, and carbon-supported Re2O7 catalysts. *Journal of Catalysis* **1985**, *93* (2), 231-245.
(118) Arnoldy, P.; Moulijn, J. A. Temperature-programmed reduction of CoOAI2O3 catalysts. *Journal of catalysis* **1985**, *93* (1), 38-54.
(119) Arnoldy, P.; Bruinsma, O.; Moulijn, J. Temperature-programmed reduction of Re2O7/Al2O3 metathesis catalysts; calculation of activation parameters for reduction. *Journal of Molecular Catalysis* **1985**, *30* (1-2), 111-123.
(120) Trejda, M.; Ziolek, M.; Decyk, P.; Duczmal, D. The radical species and impurities present in mesoporous silicas as oxidation active centres. *Microporous and mesoporous materials* **2009**, *120* (3), 214-220.
(121) Schay, Z.; Lázár, K.; Bogyay, I.; Guczi, L. Morphology and catalytic activity of iron—rhenium bimetallic catalysts supported on silica: I. Temperature-programmed reduction, x-ray photoelectron spectroscopy and Mössbauer study. *Applied catalysis* **1989**, *51* (1), 33-47.
(122) Kon, Y.; Araque, M.; Nakashima, T.; Paul, S.; Dumeignil, F.; Katryniok, B. Direct Conversion of Glycerol to Allyl Alcohol Over Alumina-Supported Rhenium Oxide. *ChemistrySelect* **2017**, *2* (30), 9864-9868.
(123) Sécordel, X.; Yoboué, A.; Berrier, E.; Cristol, S.; Lancelot, C.; Capron, M.; Paul, J.-F. Supported oxorhenate catalysts prepared by thermal spreading of metal Re0 for methanol conversion to methylal. *Journal of Solid State Chemistry* **2010**.
(124) Jehng, J.-M.; Hu, H.; Gao, X.; Wachs, I. E. The dynamic states of silica-supported metal oxide catalysts during methanol oxidation. *Catalysis Today* **1996**, *28* (4), 335-350.
(125) Kim, D. S.; Wachs, I. Surface rhenium oxide-support interaction for supported Re2O7 catalysts. *Journal of Catalysis* **1993**, *141* (2), 419-429.
(126) Nikolova, D.; Edreva-Kardjieva, R.; Kolev, H.; Gabrovska, M. Promoted Re/Al2O3 systems as sour water-gas shift catalysts. *Catalysis Today* **2020**, *357*, 590-601.

(127) Kitchin, J. *Water gas shift equilibria via the NIST Webbook*. 2013. https://kitchingroup.cheme.cmu.edu/blog/2013/02/01/Water-gas-shift-equilibria-via-the-NIST-Webbook/ (accessed 2024 08/13).
(128) Davenport, W. H.; Kollonitsch, V.; Klein, C. H. Advances in rhenium catalysts. *Industrial & Engineering Chemistry* **1968**, *60* (11), 10-19.
(129) Chauvin, Y.; Commereuc, D. Chemical counting and characterization of the active sites in the rhenium oxide/alumina metathesis catalyst. *Journal of the Chemical Society, Chemical Communications* **1992**, (6), 462-464.
(130) Lwin, S.; Wachs, I. E. Olefin metathesis by supported metal oxide catalysts. *Acs Catalysis* **2014**, *4* (8), 2505-2520.
(131) Jones, J. H. The Cativa"" Process for the Manufacture of Acetic Acid. From Zotero.
(132) Cavallo, L.; Correa, A.; Costabile, C.; Jacobsen, H. Steric and electronic effects in the bonding of N-heterocyclic ligands to transition metals. *Journal of Organometallic Chemistry* **2005**, *690* (24-25), 5407-5413. DOI: 10.1016/j.jorganchem.2005.07.012.
(133) Raab, V.; Merz, M.; Sundermeyer, J. Ligand effects in the copper catalyzed aerobic oxidative carbonylation of methanol to dimethyl carbonate (DMC). *Journal of Molecular Catalysis A: Chemical* **2001**, *175* (1-2), 51-63. DOI: 10.1016/s1381-1169(01)00220-5.
(134) Stradiotto, M.; Lundgren, R. J. *Ligand Design in Metal Chemistry*; 2016. DOI: 10.1002/9781118839621.
(135) Ping, Y.; Wang, R.; Wang, Q.; Chang, T.; Huo, J.; Lei, M.; Wang, J. Synthesis of Alkenylboronates from N -Tosylhydrazones through Palladium-Catalyzed Carbene Migratory Insertion. *Journal of the American Chemical Society* **2021**, *143* (26), 9769-9780. DOI: 10.1021/jacs.1c02331 (acccessed 2024/05/10/02:45:12). From DOI.org (Crossref).
(136) Hartwig, J. F. *Organotransition metal chemistry: from bonding to catalysis*; University Science Books, 2010.
(137) Conry, R. R.; Mayer, J. M. Low-valent rhenium-oxo complexes. 13. Rhenium(I) tris(acetylene) complexes: Re(OR')(RC.tplbond.CR)3 and [Re(L)(RC.tplbond.CR)3]OTf. *Organometallics* **1993**, *12* (8), 3179-3186. DOI: 10.1021/om00032a046 (acccessed 2024/05/10/02:34:48). From DOI.org (Crossref).
(138) Erikson, T. K. G.; Bryan, J. C.; Mayer, J. M. Low-valent oxo compounds. 5. Low-valent rhenium oxo alkoxide complexes. Synthesis, characterization, structure, and ligand exchange and carbon monoxide insertion reactions. *Organometallics* **1988**, *7* (9), 1930-1938. DOI: 10.1021/om00099a006 (acccessed 2024/05/10/02:34:28). From DOI.org (Crossref).
(139) Mayer, J. M.; Thorn, D. L.; Tulip, T. H. Synthesis, reactions, and electronic structure of low-valent rhenium-oxo compounds. Crystal and molecular structure of Re(O)I(MeC.tplbond.CMe)2. *Journal of the American Chemical Society* **1985**, *107* (25), 7454-7462. DOI: 10.1021/ja00311a039 (acccessed 2024/05/10/02:34:38). From DOI.org (Crossref).
(140) Blaszkowski, S. R.; van Santen, R. A. Theoretical Study of the Mechanism of Surface Methoxy and Dimethyl Ether Formation from Methanol Catalyzed by Zeolitic Protons. *The Journal of Physical Chemistry B* **1997**, *101* (13), 2292-2305. DOI: 10.1021/jp962006+.
(141) Boronat, M.; Martínez, C.; Corma, A. Mechanistic differences between methanol and dimethyl ether carbonylation in side pockets and large channels of mordenite. *Physical Chemistry Chemical Physics* **2011**, *13* (7), 2603. DOI: 10.1039/c0cp01996h (acccessed 2023/02/15/23:06:52). From DOI.org (Crossref).
(142) Low, J. J.; Goddard, W. A. Theoretical studies of oxidative addition and reductive elimination. 3. Carbon-hydrogen and carbon-carbon reductive coupling from palladium and platinum bis(phosphine) complexes. *Journal of the American Chemical Society* **1986**, *108* (20), 6115-6128. DOI: 10.1021/ja00280a003 (acccessed 2024/03/04/04:49:20). From DOI.org (Crossref).
(143) Culkin, D. A.; Hartwig, J. F. Carbon−Carbon Bond-Forming Reductive Elimination from Arylpalladium Complexes Containing Functionalized Alkyl Groups. Influence of Ligand Steric and Electronic Properties on Structure, Stability, and Reactivity. *Organometallics* **2004**, *23* (14), 3398-3416. DOI: 10.1021/om049726k.

(144) Tolentino, D. R.; Neale, S. E.; Isaac, C. J.; Macgregor, S. A.; Whittlesey, M. K.; Jazzar, R.; Bertrand, G. Reductive Elimination at Carbon under Steric Control. *J Am Chem Soc* **2019**, *141* (25), 9823-9826. DOI: 10.1021/jacs.9b04957 From NLM PubMed-not-MEDLINE.
(145) Daniell, W. Redox properties of Re2O7/Al2O3 as investigated by FTIR spectroscopy of adsorbed CO. *Journal of Molecular Catalysis A: Chemical* **2003**, *204-205*, 519-526. DOI: 10.1016/S1381-1169(03)00334-0 (acccessed 2023/02/17/03:09:05). From DOI.org (Crossref).
(146) Koso, S.; Nakagawa, Y.; Tomishige, K. Mechanism of the hydrogenolysis of ethers over silica-supported rhodium catalyst modified with rhenium oxide. *Journal of Catalysis* **2011**, *280* (2), 221-229. DOI: 10.1016/j.jcat.2011.03.018 (acccessed 2023/11/30/02:41:08). From DOI.org (Crossref).
(147) Shinmi, Y.; Koso, S.; Kubota, T.; Nakagawa, Y.; Tomishige, K. Modification of Rh/SiO2 catalyst for the hydrogenolysis of glycerol in water. *Applied Catalysis B: Environmental* **2010**, *94* (3-4), 318-326. DOI: 10.1016/j.apcatb.2009.11.021 (acccessed 2023/09/22/15:09:02). From DOI.org (Crossref).
(148) Koso, S.; Watanabe, H.; Okumura, K.; Nakagawa, Y.; Tomishige, K. Comparative study of Rh–MoOx and Rh–ReOx supported on SiO2 for the hydrogenolysis of ethers and polyols. *Applied Catalysis B: Environmental* **2012**, *111-112*, 27-37. DOI: 10.1016/j.apcatb.2011.09.015 (acccessed 2023/09/24/22:30:54). From DOI.org (Crossref).

Data Availability Statement

The authors declare that the data supporting the findings of this study are available within the paper, its supplementary information files, and can be obtained from the corresponding author on reasonable request.